

DYAMOND: the DYnamics of the Atmospheric general circulation Modeled On Non-hydrostatic Domains

Article

Published Version

Creative Commons: Attribution 4.0 (CC-BY)

Open Access

Stevens, B., Satoh, M., Auger, L., Biercamp, J., Bretherton, C. S., Chen, X., Düben, P., Judt, F., Khairoutdinov, M., Klocke, D., Kodama, C., Kornblueh, L., Lin, S.-J., Neumann, P., Putman, W. M., Röber, N., Shibuya, R., Vanniere, B. ORCID: <https://orcid.org/0000-0001-8600-400X>, Vidale, P. L. ORCID: <https://orcid.org/0000-0002-1800-8460>, Wedi, N. and Zhou, L. (2019) DYAMOND: the DYnamics of the Atmospheric general circulation Modeled On Non-hydrostatic Domains. *Progress in Earth and Planetary Science*, 6. 61. ISSN 2197-4284 doi: 10.1186/s40645-019-0304-z Available at <https://centaur.reading.ac.uk/86813/>

It is advisable to refer to the publisher's version if you intend to cite from the work. See [Guidance on citing](#).

To link to this article DOI: <http://dx.doi.org/10.1186/s40645-019-0304-z>

Publisher: Springer

including copyright law. Copyright and IPR is retained by the creators or other copyright holders. Terms and conditions for use of this material are defined in the [End User Agreement](#).

www.reading.ac.uk/centaur

CentAUR

Central Archive at the University of Reading


Reading's research outputs online

REVIEW

Open Access



DYAMOND: the DYnamics of the Atmospheric general circulation Modeled On Non-hydrostatic Domains

Bjorn Stevens^{1*} , Masaki Satoh², Ludovic Auger³, Joachim Biercamp⁴, Christopher S. Bretherton⁵, Xi Chen⁶, Peter Düben⁷, Falko Judt⁸, Marat Khairoutdinov⁹, Daniel Klocke¹⁰, Chihiro Kodama¹¹, Luis Kornbluh¹, Shian-Jiann Lin⁶, Philipp Neumann⁴, William M. Putman¹², Niklas Röber⁴, Ryosuke Shibuya¹¹, Benoit Vanniere¹³, Pier Luigi Vidale¹³, Nils Wedi⁷ and Linjiong Zhou⁶

Abstract

A review of the experimental protocol and motivation for DYAMOND, the first intercomparison project of global storm-resolving models, is presented. Nine models submitted simulation output for a 40-day (1 August–10 September 2016) intercomparison period. Eight of these employed a tiling of the sphere that was uniformly less than 5 km. By resolving the transient dynamics of convective storms in the tropics, global storm-resolving models remove the need to parameterize tropical deep convection, providing a fundamentally more sound representation of the climate system and a more natural link to commensurately high-resolution data from satellite-borne sensors. The models and some basic characteristics of their output are described in more detail, as is the availability and planned use of this output for future scientific study. Tropically and zonally averaged energy budgets, precipitable water distributions, and precipitation from the model ensemble are evaluated, as is their representation of tropical cyclones and the predictability of column water vapor, the latter being important for tropical weather.

Keywords: Climate modeling, Model intercomparison project, Tropical convection, Convective parameterization

Introduction

About 20 years ago, Taroh Matsuno proposed to develop a global non-hydrostatic model as a demonstrator project for the Earth Simulator, a Japanese supercomputer that was being developed to be the most powerful of the world at that time (Matsuno 2016). His idea was to provide a tropical analogue to the mid-latitude numerical experiments of Phillips (1956) and Smagorinsky (1963)—one that could resolve the transient dynamics of tropical deep convection, and its various forms of organization. Doing so required a global grid, and a formulation of the governing equations, that would permit motions on scales of 5 km. Such approaches, long common place on smaller domains¹, became conceivable globally

with the ambitious development of the Earth Simulator (Satoh et al. 2005). These efforts bore fruit, in the form of new numerical methods (Tomita et al. 2001; Tomita and Satoh 2004) and the first ever aqua-planet simulations using a global non-hydrostatic model called NICAM (Tomita et al. 2005; Satoh et al. 2008; Satoh et al. 2014). NICAM, which has since been applied to more realistic planetary configurations and a great variety of questions (see reviews by Satoh et al. 2017, 2018, 2019), demonstrated the ability of a model to use unfiltered equations of atmospheric motion, on a global domain, to represent convective storms in the tropics as a component of the general circulation.

In the years since the introduction of NICAM, a small number of groups initiated similar efforts to use the continuing growth in computational capacity (e.g., Putman and Suarez (2011)) to enable the simulation of the atmospheric general circulation on non-hydrostatic domains (Satoh et al. 2019). These groups, coming from

*Correspondence: bjorn.stevens@mpimet.mpg.de

¹ Max Planck Institute for Meteorology, Bundesstraße 53, 20146, Hamburg, Germany

Full list of author information is available at the end of the article

¹ By the early 2000s, approaches pioneered by Cotton and Tripoli (1978) and Klemp and Wilhelmson (1978) had become operational (Saito et al. 2007).

different modeling traditions—weather prediction, data assimilation, mesoscale meteorology, and climate science, shared a common purpose. By explicitly simulating how small and intermediate scales of motions couple to large-scale circulation systems, they sought to circumvent considerable, and seemingly intractable, problems arising from parameterizations—particularly of deep convection (Randall et al. 2003; Stevens and Bony 2013). Models with this capacity—which we call global storm-resolving models (or GSRMs)—are providing the foundation for a new generation of weather and climate models. Their use will shine welcome new light on long-standing questions, such as how tropical rainbands, or other patterns of weather, change with warming (Bony et al. 2015; Marotzke et al. 2017).

An important next step in the application of such models is to begin identifying which aspects of the simulated climate system are independent of the details of the GSRM implementation. Separating robust (implementation independent) from non-robust features is most easily done through a controlled program of model intercomparison. Such an intercomparison helps shape expectations and guide future developments in at least three ways: (i) by identifying and helping resolve what should be trivial problems, such as apparent implementation bugs; (ii) by focusing efforts on non-trivial problems, for instance the representation of turbulent mixing and cloud microphysical processes, or managing and efficiently analyzing output; and (iii) by involving a larger community in the excitement of exploring the behaviors of a new class of models. Toward these ends, we have initiated the first intercomparison of GSRMs, through a project we call DYAMOND—the DYnamics of the Atmospheric general circulation On Non-hydrostatic Domains².

The aim of this paper is to describe DYAMOND and present first results. The selection of what to present was guided by a desire to illustrate promising directions of analysis that have emerged from initial explorations of the output, and to make a first identification of issues for the further development of this simulation capability. To accomplish our aim the remainder of this paper is organized as follows: The DYAMOND experimental protocol is presented in the “[Experimental protocol](#)” section. In the “[Models](#)” section, we present the nine models which contributed simulation output to DYAMOND, including some characteristics of their computational performance and a brief description of the output they provide. In the “[Simulations](#)” section some characteristics of the simulations are presented by way of overview, complemented by snapshots to help motivate subsequent work by a broader

community. We conclude with a summary and our ideas regarding future steps.

Experimental protocol

The DYAMOND protocol specified a simulation of 40 days and 40 nights, beginning at 0Z, 1 August 2016, using global models with a grid spacing of 5 km or less. The global (9 km) meteorological analysis taken from the European Centre for Medium Range Weather Forecasts (ECMWF) was used to initialize the atmospheric state. ECMWF operational daily sea-surface temperatures and sea-ice concentrations were also used as initial and boundary data. These input fields are archived and made available as part of the DYAMOND dataset. Models were left free to formulate their own initialization of the land surface and adopted a variety of strategies for this purpose. ICON, for instance, took soil moisture from ECMWF and converted to a soil moisture index (SMI) which was then vertically interpolated to the ICON soil level SMI and soil temperature which it then converted back to soil moisture using ICON’s soil characteristics. MPAS used the NOAA-MP land model and initialized it with ERA5 surface data from 1 August 2018, and other models, such as the UKMO, used soil moisture taken from previous, lower-resolution runs. Perhaps because the resolution of the analyses used for initialization was relatively fine, no groups reported special problems with the initialization, even if spurious gravity waves are expected to arise from topographic and other mismatches.

The DYAMOND protocol was kept as simple as possible to encourage participation and ensure a fast turnaround. For this reason, what, how much, and in what form the output was to be provided was left for participating groups to decide for themselves. Instead of specifying output data requirements, groups communicated which output they were writing in the case that could help guide the choices of other groups. Ways of dealing with different naming conventions, grids, units, etc. were things the project aimed to explore in post-processing, in part to guide development of domain-specific analysis languages, like the Climate Data Operators (CDO). From this perspective, having each group’s native format as output was actually advantageous. Expediency was also the reason why no attempt was made to coordinate and homogenize the initialization of the land surface. This expedient approach achieved its aims. The idea of DYAMOND arose in October 2017, during a workshop of the cloud-feedback intercomparison project in Tokyo, the outline of the experimental specifications was drafted at the end of November of the same year, and eight of the nine participating groups had finished their runs and (mostly) uploaded the data before a year had passed.

²<https://www.esiwave.eu/services/dyamond>

The initialization date (1 August 2016) was motivated by the possibility of linking to previous large-domain storm-resolving model simulations performed in support of field work over the Northern Atlantic (Klocke et al. 2017; Stevens et al. 2019). The coincidence of this period with the boreal monsoon, the active part of northern hemispheric tropical cyclone season, and the good satellite coverage were further motivations. Simulating 40 days and 40 nights had a symbolic motivation, as in some ancient cultures it denotes an eternity, and a practical motivation, as it allowed for a comparison of 30 days (1 month) after a 10-day spin-up. Through this, it was hoped to crudely separate questions of predictability from questions of climatology.

Models

Structure and configuration

Most of the DYAMOND models (Table 1) solve the fully compressible Navier-Stokes equations, with their representation of molecular diffusion modified to account for unresolved turbulent motions and for an atmosphere with a condensable (water) component. Exceptions are the System for Atmospheric Modeling (SAM) which uses the anelastic form of the non-hydrostatic equations and the Integrated Forecast System (IFS) which uses the (hydrostatic) primitive equations and is thus the only hydrostatic model. More generally, the numerical methods used by the different models to solve their governing equations depend on their choice of grid and a number of other factors, and thus vary considerably. These differences contribute to the richness of the simulation dataset as a basis for assessing the importance of model formulation choices. Table 1 provides technical references for the participating models.

The configuration of the numerical grid over which each model solves its governing equations, and some parameters indicative of how these equations are structured, is given in Table 2. A diversity of grids—many of which are

reviewed by Williamson (2007)—are employed across the DYAMOND models. FV3 and GEOS5 share a dynamical core based on a cubed sphere, NICAM and ICON use an icosahedral grid as a starting point for their discretization, and MPAS employs spherical centroidal Voronoi tessellation. The IFS operates with a cubic octahedral (Gaussian) reduced grid with T2559 truncation in spectral space, and the ARPEGE-NH uses an alternative Gaussian reduced grid with the truncation T8000 in spectral space. The UM and SAM use latitude-longitude grids, which introduce more severe numerical challenges as they are refined. For SAM, as it was implemented for DYAMOND, a columnar (wall) boundary pierces the sphere and bounds the flow to lie equatorward of 89° latitude. For the UM, no special accommodation for the pole was introduced except to use a somewhat coarser tiling of the sphere (see Table 2) as compared to the other models.

The DYAMOND models differ more substantially in their choice of vertical coordinates, thermodynamic variables, and how parameterizations are used to represent processes that would otherwise be inadequately represented. Table 2 also gives a flavor of these differences; more detailed descriptions are provided in each model's technical documentation (Table 1). Notably models differed in how they treated convective parameterization, especially shallow convection, perhaps reflecting a lack of consensus as to how much of the convection would be explicitly resolved at the target grid spacing.

The choice of vertical coordinate influences the stability of the model in regions of steep topography and the representation of the topography itself. Figure 1 visualizes a subset of the DYAMOND models in the vicinity of Mt. Fuji to illustrate these differences. It emphasizes that the number of levels is not the only consideration when evaluating the vertical resolution among the different models. Differences in the surface orography manifest themselves not only in the height and steepness of mountains, but also on the shape of the coastline, and the extent to which some features (small islands) are even represented.

The vertical span of the model grids and the number of levels over which they are discretized also vary (Table 2), and most models employ some form of damping as their upper boundary is approached. For example, in the case of ICON, this damping is applied to the levels between 44 km and the model top, which is at 75 km.

Output

A simple calculation illustrates the magnitude of the output challenge posed by GSRMs. Taking ICON as an example, a state vector of 11 variables (5 microphysical variables, 3 components of the velocity vector, and 3 thermodynamic coordinates) with 84×10^6 horizontal and 90 vertical degrees of freedom (Table 2) comprises

Table 1 DYAMOND models

Name	References
ARPEGE-NH	Bubnová et al. (1995), Voldoire et al. (2017)
FV3	Lin and Rood (2004), Lin (2004)
GEOS5	Putman and Lin (2007), Putman and Suarez (2011)
ICON	Zängl et al. (2014), Hohenegger et al. (2019)
IFS	Wedi (2014), Malardel et al. (2016)
SAM	Khairoutdinov and Randall (2003), Satoh et al. (2019)
MPAS	Skamarock et al. (2012, 2014)
NICAM	Satoh et al. (2008, 2014)
UM	Wood et al. (2013), Walters et al. (2017)

Short names for models submitting output to DYAMOND and references to recent scientific documentation for each model

Table 2 Configuration of the DYAMOND models

Name	Grid	#Mcol	#lev	# μ	$\sqrt{A_{\max}}$	H_{top}	H_{spong}	CP	BL	FC
ARPEGE-NH	Kurihara	82	75	5	2.5 km	70 km	34 km	N	T	Yes
FV3	Cube	57	79	6	3.3 km	39 km	25 km	S	K	Yes
GEOS	Cube	57	132	5	3.3 km	80 km	75 km	F	K	Yes
ICON	Icoso	84	90	5	2.5 km	75 km	44 km	N	T	Yes
IFS	Octo	26	137	5	4.8 km	80 km	65 km	S	K	Yes
MPAS	Voronoi	42	75	6	3.8 km	40 km	30 km	F	T	Yes
NICAM	Icoso	42	78	5	3.5 km	50 km	25 km	N	K	No
SAM	La-Lo	43	74	5	4.3 km	37 km	22 km	N	S	No
UM	La-Lo	20	85	6	7.8 km	85 km	42 km	S	K	Yes

Tabulated are the number of columns (#Mcol, in millions), the vertical levels (#lev, not counting soil levels), the microphysical variables (# μ), the linear dimension of the area, the A of the largest tile ($\sqrt{A_{\max}}$), the vertical span of the column (H_{top}), and the height (H_{spong}) where the sponge layer begins. The last three columns denote parameterization assumptions. For cumulus parameterization (denoted CP), the letters "N," "S," and "F" denote none, shallow, or full parameterization, whereby for the latter, some assumptions are usually included in an attempt to account for the scale of motions being parameterized. For the boundary layer parameterization (denoted BL), the letters "T," "K," and "S" denote either a TKE-like model (including an additional prognostic equation), a diagnostic eddy diffusivity, or a Smagorinsky-like three-dimensional closure as is common for large-eddy simulation. Finally, some indication is given as to whether fractional cloudiness (denoted FC) is parameterized

nearly a terabyte of information (664 GBytes, double precision) per sample. Hourly output for 40 days inflates this by a factor of a thousand. The practice of providing derived variables, e.g., measuring energy and matter fluxes, inflates this by another factor of 3. Hence, approaching the output naively would imply data volumes of about 2 PBytes for each model. This contextualizes one motivation for DYAMOND, which was to develop strategies for dealing effectively with the large amount of information inherent in GSRMs. For this reason, groups were encouraged to approach the problem as they saw fit, with the idea that the sharing of approaches would help guide the development and uptake of best practices.

All groups used a hierarchical approach, with more frequent output of 2D variables and less frequent output of 3D fields. Most groups limited 3D output to a fairly small elaboration of their state vector at 3 h intervals. Some two-dimensional output was written to disk by most models every 15 min, every 30 min for SAM, and every 60 min for the IFS. To avoid unnecessary repetition in output, many models, usually those with a less regular grid structure (i.e., ICON, FV3, and MPAS), provided grid information in a stand-alone file which must be specified when reading the data. NICAM and GEOS fall into this category, but only distributed output after it had been remapped to a regular grid. All groups provided output in some flavor of GRIB or NetCDF, and many groups employed some form of compression before writing output to disk. Compression saves space, but slows access to the data, which must be decompressed before use. This issue was especially evident when accessing ICON output, which was written using the GRIB2 standard and a second level of compression. This approach reduced the output file volumes by

a factor of 5, but because the second-level decompression did not multi-thread well, access to the output was considerably slower. This experience has since motivated task-parallel optimization developments to improve the decompression step, but is a reminder that compressed formats involve trade-offs.

The simulations provide a lot of samples of mesoscale convective systems, whose statistical characteristics can be analyzed. To aid exploration of the output, a standardized set of (two-dimensional) information (Table 3) was post-processed for each model. The processing consisted of interpolating the variables to a common 0.1° grid (using a conservative remapping via the remap function of CDO version 1.9.5) and saving, for each time level of each model's output, the data as a netCDF (version 4) file. The remapped output of model variables was averaged over the full 40-day period, as well as over the last 30, 20, and 10 days, leading to 4 time-averaged output files on the same 0.1° grid for each model. To ensure consistency between the remapped and source output, and because the number of participating models is small, the data provided on the 0.1° grid retain the same variable name, and units, as the original model output.

The sheer size of the output fields also poses quite a challenge for their visualization. Even in the cases where we might be able to visualize model output using relatively conventional approaches, to interactively explore and visually analyze the full 3D data set over time, would require parallel visualization techniques. For yet larger simulations, in situ visualization techniques and/or an online compression and a level-of-detail (LoD) rendering approach (Jubair et al. 2016; Bethel et al. 2012; Clyne et al. 2007) would also be necessary.

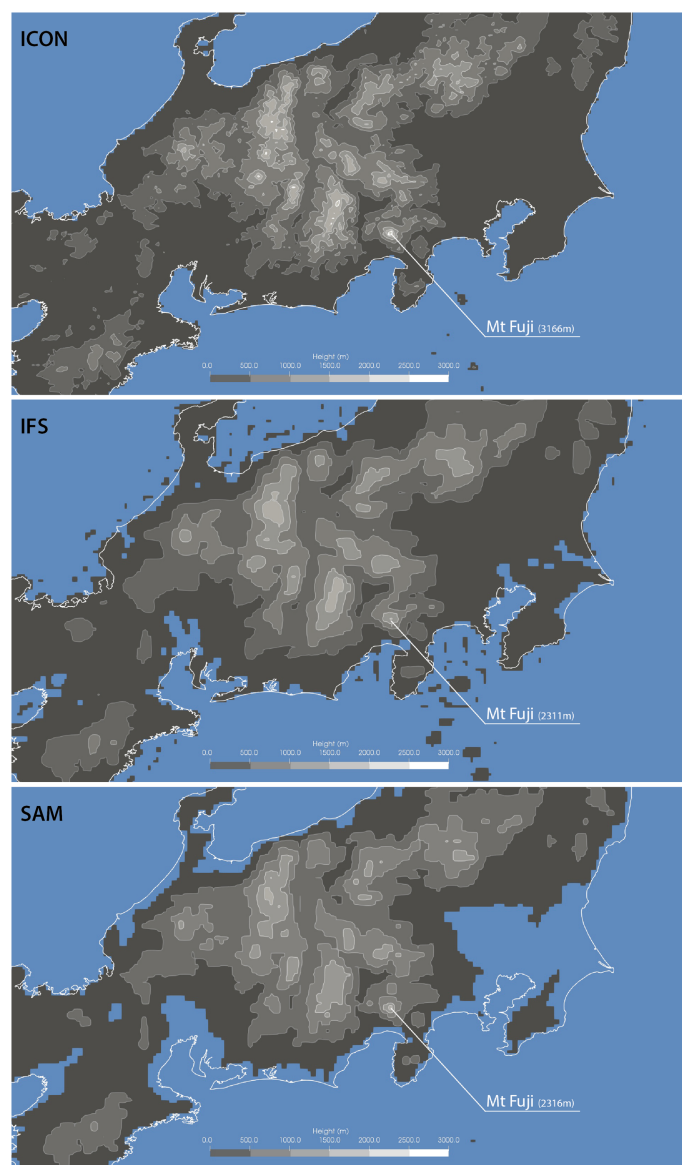


Fig. 1 Orographic boundary conditions around the region of Mt. Fuji (3776 m). Plotted is the height of the surface, relative to mean sea level, taken from ICON, IFS, and SAM to illustrate different representations of topography. Note that the land-sea mask does not correspond to the height of the 0 m contour, so even if regions may formally be just above, respectively below, sea level, this does not preclude them from being treated as sea, respectively land

The German Climate Computing Center (DKRZ) agreed to host the output and serve as an analysis hub for the community, something made possible through close interaction with a European Commission funded Centre of Excellence in Simulation of Weather and Climate in Europe—the ESiWACE project.

An accidental ensemble

There is a temptation to question what can be learned about the climate system from a single 40-day snapshot.

Experience suggests a great deal. For instance, Rodwell and Palmer (2007) showed how initial tendency errors—identified in a data-assimilation procedure—are informative of model biases. Simpler approaches, using hindcasts, have shown to be similarly indicative of climatological biases (Williamson 2005; Williams et al. 2013).

Quite apart from this backdrop, DYAMOND provides an additional means for testing to what extent differences among models are significant. It does so by including in the DYAMOND dataset an accidental ensemble

Table 3 Homogenized output variables

Quantity
Precipitation (rate) at the surface
Column integrated total water
Column integrated liquid water
Column integrated solid water (ice)
Net terrestrial radiation (at TOA and surface)
Net TOA solar radiation (at TOA and surface)
Pressure (interpolated to sea level)
Zonal wind speed (at 10 m)
Meridional wind speed (at 10 m)
Temperature (at 2 m)

Each model's variables were remapped to a regular 2D LaLo grid, and these were in turn time-averaged for four different periods. The remapping was done to ensure that, at a minimum, the following information was available for each model

of additional simulations. These include simulations performed with the identical model but at progressively lower resolution, simulations with different parameter settings, and simulations with what was later deemed to be undesirable treatments of boundary or initial data. Table 4 describes the additional DYAMOND simulations that have been archived and made available as part of this ensemble. So for instance based on this table, simply by comparing an ICON simulation run at 5 km with a simulation run in the base configuration and comparing it to another model run at its base configuration, one can begin to assess to what extent differences between the models are likely to be systematic.

Computational performance

To aid efforts to assess (and eventually enhance) the computational efficiency of GSRMs, groups were asked to specify some computational details of their calculations. These are provided in Table 5. The information in the table is difficult to interpret without expertise in the different computational architectures on which the models were run. It is also colored by the different levels of effort groups have put into optimizing the porting of their model to their particular computing environment. The structure of the model itself also influences the interpretation of these numbers; for instance, most models use different time-integration schemes, or different timesteps, for marching different processes forward in time. Because it usually sets the pace, the shortest timestep (usually used to represent sound waves) is also listed in Table 5.

Notwithstanding these caveats, some general conclusions can be drawn. One is that the throughput of the DYAMOND models on a $\mathcal{O}(3)$ km mesh was about 6 SDPD (simulated days per day) on a modest fraction of the host-machine nodes (ICON was run on one

Table 4 Accidental ensemble

Name	A_{\max}	Salient (additional) difference
FV3	6.5 km	Three member ensemble
GEOS5	6 km	None
ICON	5 km	None
"	10 km	"
"	20 km	"
"	40 km	"
"	80 km	"
"	20 km	Full NWP physics (convective parameterization)
"	40 km	"
"	80 km	"
"	5 km	DWD grid
"	5 km	DWD grid, erroneous specification of surface albedo over Asia
"	5 km	Fixed SST (to value on 1 August)
IFS	9km	TCo1279 near-operational configuration, with fully active convective parametrization
MPAS	7 km	None
"	3.5 km	With fully active convective parameterization
"	7.0 km	"
NICAM	7 km	None
"	14 km	"
UM	15 km	None
ECHAM6	100 km	T127 (100 km) ten-member ensemble with full parameterization

Salient information about additional simulations performed by various groups and made available as part of the DYAMOND archive

sixth of the DKRZ machine Mistral). IFS, representing a large class of existing global numerical weather prediction models (Mengaldo et al. 2018), operates at a higher SDPD, in part due to the numerical scheme allowing the stable use of larger timesteps and the use of single precision. Similar time-stepping procedures were used by the UM and ARPEGE-NH, but did not permit as large a timestep as was possible for the hydrostatic implementation of the IFS. With increasing vertical accelerations, some of the numerical simplifications that enable a large throughput for models like the IFS come into question. Results made available by DYAMOND will foster research on the numerical and algorithmic trade-offs on scales where non-hydrostatic accelerations may become important.

Many of the DYAMOND models were run also at coarser resolution, as discussed above, and this aided an assessment of parallel scalability. The more coarsely resolved configurations showed that the models were still scaling excellently, consistent with the relatively large amount of computational intensity per computational

Table 5 Computational aspects

Model	Nodes	Cores	SDPD	Δt	Processor (date of launch into market)
ARPEGE-NH	300	7200	2.6	100 s	Intel Xeon "Ivy Bridge" (2013)
FV3	384	13,824	19	4.5 s	Intel Xeon "Broadwell" (2016)
GEOS	512	20,480	6.2	3.75 s	Intel Xeon "Skylake" (2017)
ICON	540	12,960	6.1	4.5 s	Intel Xeon "Haswell" (2014)
IFS	360	12,960	124	240 s	Intel Xeon "Broadwell" (2016)
MPAS	256	9216	3.5	10 s	Intel Xeon "Broadwell" (2016)
NICAM	640	2560	2.6	10 s	NEX SX-ACE vector processor (2015)
SAM	128	4608	6.0	7.5 s	Intel Xeon "Broadwell" (2016)
UM	340	12,240	6.0	90.0 s	Intel Xeon "Broadwell" (2016)

To give a rough idea of the performance of the different models, their throughput is given and contextualized by some basic information about architectures on which they were run. Columns indicate the number of nodes, the total number of cores on which the simulations were run, the simulated days per day, the shortest (usually acoustic) timestep (Δt), and the type of processor

element at the given limited core counts; most models typically have a column-to-processing-element ratio of about 10^4 . From this, we conclude that even without confronting disruptive changes that stand in the way of achieving yet greater gains, a factor of 10 to 15 in computational throughput in a 5-year period will be achievable. Such an increase would enable global simulations on a 3-km grid with throughput of about 100 SDPD and hence allow these approaches to be applied to a broader class of climate change questions. It also makes global LES, with simulations of a few days on a 300-m grid, conceivable. The latter could be used to target some of the—not inconsiderable—simulation uncertainties that remain in GSRMs, since fully resolving shallow cloud systems, whose vertical (and hence horizontal) scale may be only a few kilometers, requires substantially smaller grid distances.

Simulations

"Palmer-Turing" test

In an essay on modeling the climate system, Palmer (2016) introduced the notion of using Alan Turing's test as a measure of climate model fidelity. Turing's original idea was to use the extent to which a passive observer could distinguish a conversation between a human and a computer from a conversation between two humans as a measure of artificial intelligence. Palmer's variant of Turing's test is presented in Fig. 2, which compares a snapshot of the Earth from a geostationary satellite, with a visualization of its condensate burdens using output from the nine DYAMOND models. A second simulation by the IFS, at its operational resolution, is also included as a further reference. The visualizations are created using the condensate output of the models and rendered through the 3D visualization software ParaView in a way to visually mimic the true color output of the Himawari 8 reference data. The Rayleigh scattering of the atmosphere was thereby

imitated by the rendering process. White color is used for both cloud water and cloud ice, along with a zero to one clamped weighted logarithmic opacity table that is adjusted to the data ranges of each model and by visual comparison to the Himawari 8 reference data. On a superficial level, the fact that the image of Himawari 8 (Bessho et al. 2016) is not distinguishable from the model output suggests that the simulations pass, at least in a weak form, the "Palmer-Turing" test.

Himawari 8 was chosen as the basis for comparison because it was the most advanced geostationary satellite in orbit in 2016. The images are constructed from the output at 0400 UTC on 4 August 2016, which corresponds to 10:37:12 local time at 140.7° E where Himawari 8 is located and the images are centered. At this time, the models still are on trajectories that are well constrained by the atmospheric state from which they were initialized, 76 h previously. This fact is reflected in the similarity in the positioning of large-scale circulation features, such as the band of tropical convection stretching from the center of the image to the east-northeast, a band of convection stretching across China, and frontal systems extending along the east and west coasts of Australia. Many of the models capture the tripole-like structure of the band of tropical convection, whose most developed and westward feature was associated with a developing tropical cyclone that was classified as typhoon Omais by the Japanese Meteorological Agency later in the day. They also well represent the absence of convection and its wave-like structure in the central equatorial Pacific.

Though largely qualitative at this point, a striking aspect of Fig. 2 is how different each image is in the visualization of its condensate, despite the apparent realism of each one of them. These differences are most apparent away from regions of large-scale organized motion and are illustrated by zooming over specific regions and

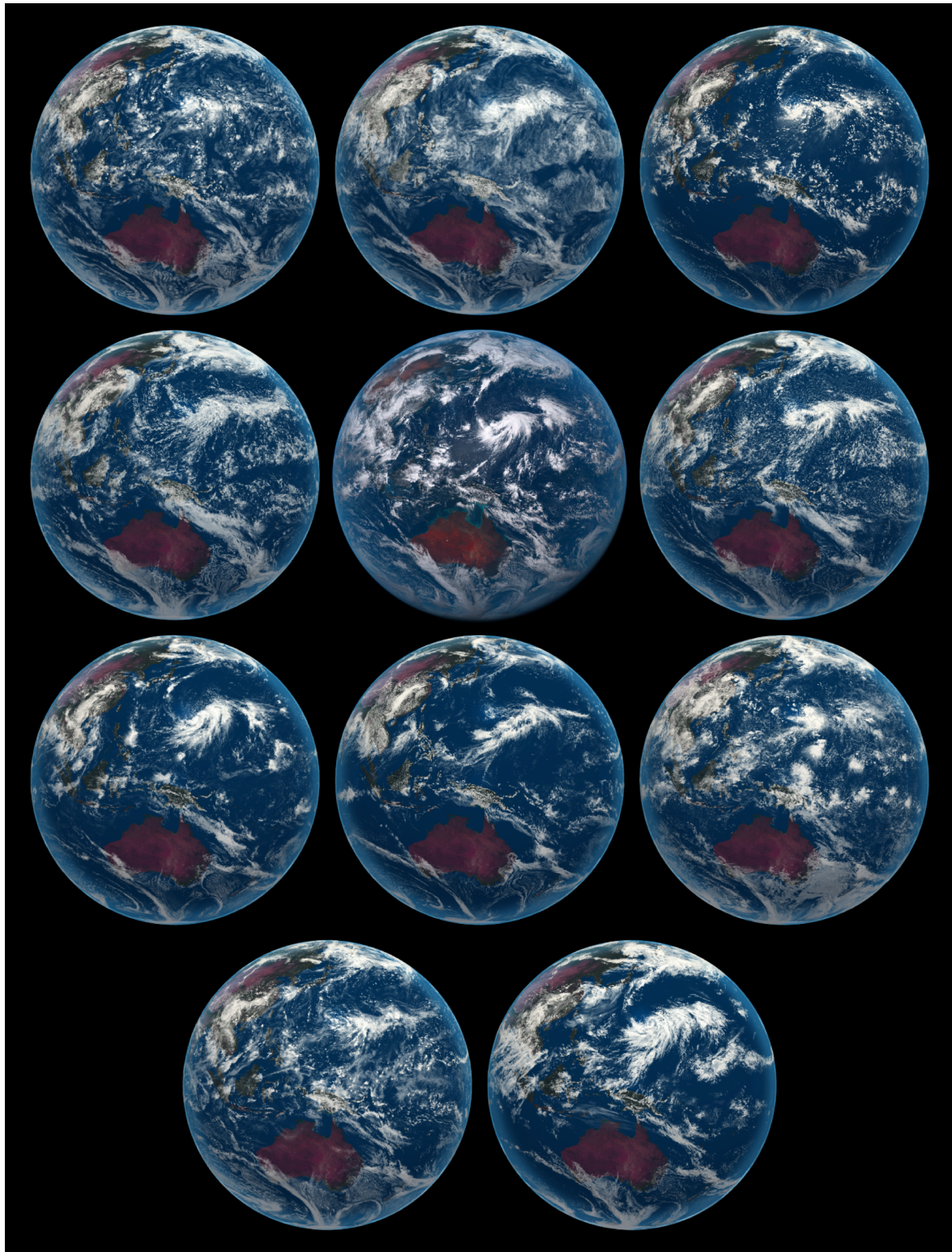


Fig. 2 Snapshot of DYAMOND models. A snapshot of the models taken from the perspective of the Himawari 8 is shown. The images are for the cloud scene on 4 August 2016 and are qualitatively rendered based on each model's condensate fields to illustrate the variety of convective structures resolved by the models and difficulty of distinguishing them from actual observations. From left to right: IFS-4 km, IFS-9 km, and NICAM (top row); ARPEGE, Himawari, and ICON (second row); FV3, GEOS5, and UKMO (third row); and SAM and MPAS (bottom row)

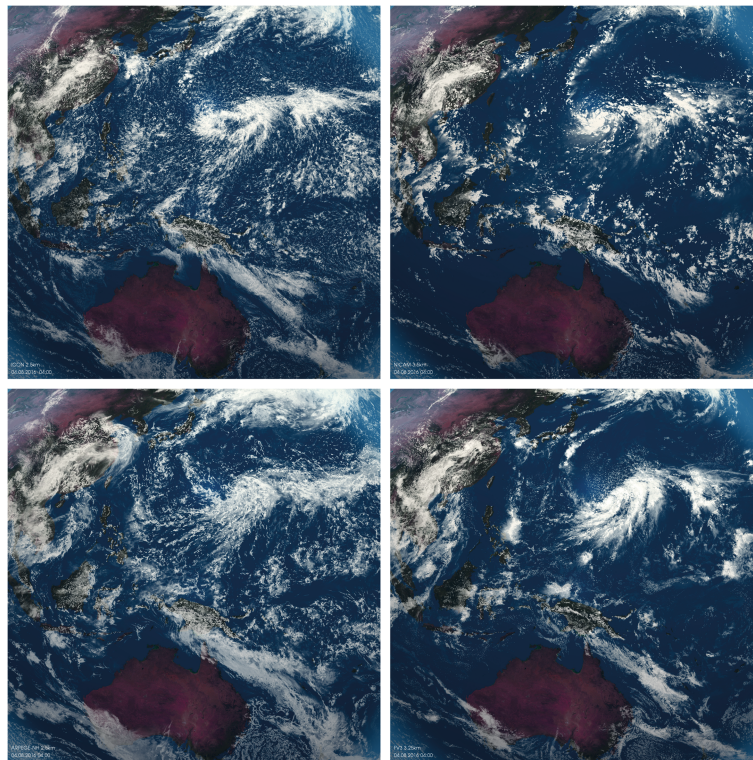


Fig. 3 Zoom of Fig. 2 highlighting the structure of tropical cloud fields in the vicinity of Omais, which was named and classified as a tropical cyclone on this day

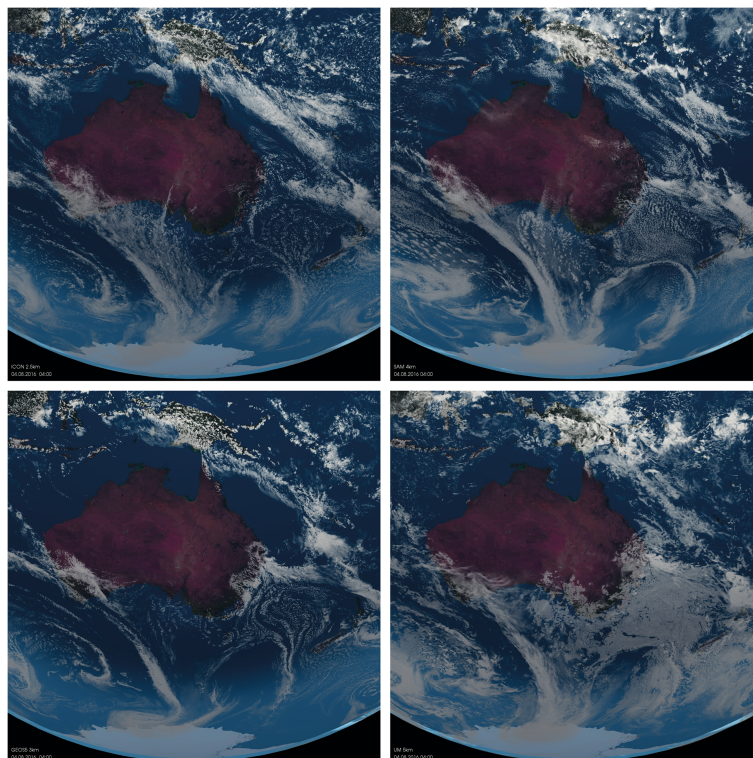


Fig. 4 Zoom of Fig. 2 highlighting the structure of post-frontal low cloud fields south and east of Australia

examining the visualization of a subset of the models. One such zoom is centered over the feature that is developing into typhoon Omais in the central Pacific (Fig. 3). The second zoom is centered on Australia to highlight the structure of the shallower cloud field between Australia and New Zealand, in the cold sector of an extra-tropical cyclone (Fig. 4). The major difference between the simulations in the left panels of Fig. 3, and those shown in the right panels is the structure of the reflectivity features away from regions of deep convection, which we interpret as arising from condensate loading in shallower convection (see also Fig. 4). The images suggest that despite capturing the patterning of large-scale circulation features on the distribution of condensate, which is what structures the images and gives them their apparent “realism,” substantial differences become apparent when looked at quantitatively. These differences are likely sensitive to the representation of both cloud microphysics and shallow convection, whose treatment differs across the models.

Precipitation

Among the fields expected to be better represented by GSRMs, precipitation stands out as being of particular interest. This special status arises not only from theoretical considerations, but also from experience. A number of studies, e.g., Weisman et al. (1997), Langhans et al. (2012), Ito et al. (2017), Hohenegger et al. (2019), Stevens et al. (2019), show that bulk precipitation statistics converge—at least on regional scales—with grid spacings of 1 to 4 km. Convergence has been less explored on global storm-resolving scales (cf Hohenegger et al. (2019)) and never across a model ensemble. It is something that we begin to investigate with the DYAMOND simulations.

We start by comparing zonally and temporally averaged precipitation from the last 30 days of the DYAMOND simulations. This comparison is presented in Fig. 5, which also includes precipitation estimated from observations for the same time period. The analysis by Kodama et al. (2012) identified a spin-up period of a few days in 14 km NICAM simulations. By discarding the initial 10 days, we thus avoid undue constraints from the initialization, as well as biases from differences in how the different models spin-up. The comparison is nonetheless susceptible to a poor sampling of internal variability. To get a sense of the magnitude of the sampling error that may be associated with this variability, we calculate the week-to-week standard deviation of the zonally averaged precipitation. It is about 15 % of the mean (or similar to the variability among the models) and does not vary systematically from model to model, or as a function of latitude. Being mindful of the sampling precision, Fig. 5 highlights the agreement among a large subset of the simulations in

terms of their representation of the zonally and globally averaged precipitation. Their tropical averaged precipitation for the final 30 days of the simulation is $3.813 \pm 0.164 \text{ mm d}^{-1}$ (1-sigma). ARPEGE-2.5 km simulates clearly larger precipitation (4.25 mm d^{-1}) as compared to the main group of models. This difference is believed to be the result of an artificial increase in surface evaporation which had been introduced into the lower resolution version of the model to improve its representation of tropical cyclone intensity, and for this reason, ARPEGE-2.5 km has been excluded from the subset. As discussed later, this also is believed to be responsible for ARPEGE-2.5 km producing much more intense tropical cyclones and also a much moister atmosphere, thus forming an interesting natural experiment. GEOS-3.3 km produces much less (3.2 mm d^{-1}) precipitation. This appears to be related to an output error, and a new set of simulations has been performed for inclusion in subsequent analysis. At the time of our analysis, however, this data was not available, so GEOS-3.3 km is not included in either the tabulation or the computation of the multi-model mean.

Compared to the cluster of models in Fig. 5, the observed precipitation (3.50 mm d^{-1}) for the same period—as estimated from calibrated microwave measurements to retrieve precipitation globally at 10 km spatial and hourly temporal scales—is at the two-sigma range of this group of models. The observations and models differ by an amount that is larger than the week-to-week variability just south of the Equator, where the simulations have a secondary peak in precipitation that is more pronounced than is observed, and in the very high latitudes of the Southern Hemisphere. The greater than observed precipitation just south of the Equator may represent a bias of the models, akin to the double ITCZ bias that is familiar from models of parameterized convection, or may be indicative of a deficiency in the observational retrievals in capturing what can often be intense precipitation from relatively isolated warm (congestus) clouds. Discrepancies at high latitudes are within the range of other observational products, e.g., the IMERGE product retrieves twice as much precipitation at 50°S as compared to GSMaP.v7 (Hiro Masunaga, Yukari Takayabu, personal communication, 2018; GSMaP: Kubota et al. (2007)). Differences in the observed global mean and that simulated by the subset of models in Fig. 5 cannot however be explained by differences at high latitudes.

Quantities related to the tropical (equatorward of 30°) water and energy budgets are summarized in Table 6. In addition to precipitation, the 30-day means for precipitable water and both outgoing terrestrial and absorbed solar irradiances are presented. We focus on the tropics because this is the region where convective heat transport

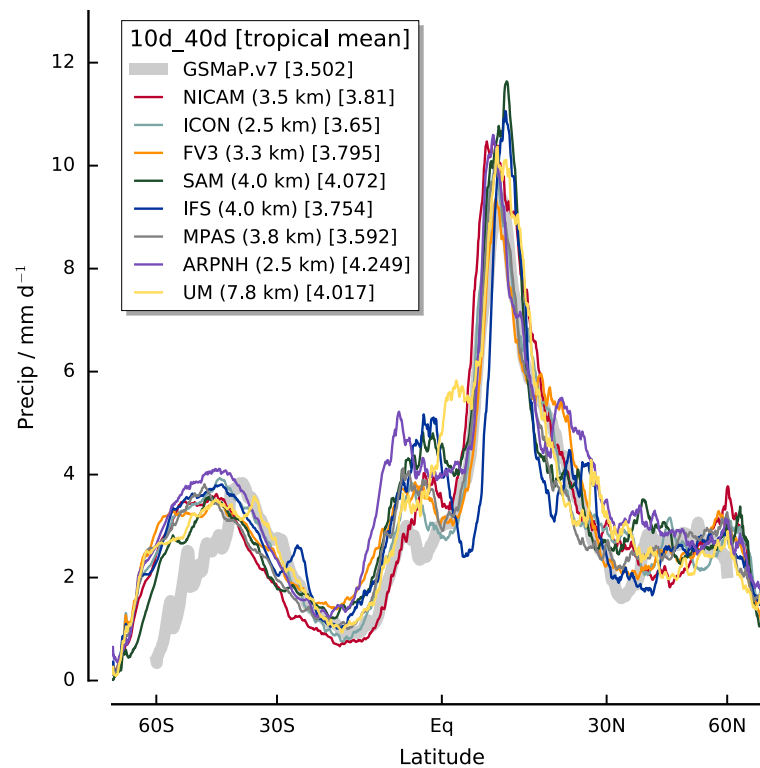


Fig. 5 Mean precipitation. Precipitation is zonally and temporally averaged (over the last 30 days of the simulation) for each of the indicated models. The global averaged precipitation for each model is indicated in the legend. Mean precipitation from the GSMaP project (version 7) is provided as a reference. The GSMaP line width is to distinguish it from the models, not a measure of retrieval uncertainty

Table 6 Tropical budgets

Model	P mm d ⁻¹	PW mm	I_{thermal} W m ⁻²	I_{solar} W m ⁻²
ARPEGE-NH	4.25	40.9	-265.4	319.3
FV3	3.80	38.7	-269.0	307.6
GEOS	n/a	39.5	-269.2	303.1
ICON	3.65	38.8	-264.1	295.2
IFS	3.75	35.4	-268.4	312.2
MPAS	3.59	37.1	-265.9	327.3
NICAM	3.81	41.5	-259.2	327.0
SAM	4.07	37.3	-272.3	311.7
UM	4.02	38.1	-267.4	309.0
Observed	3.50	39.5	-259.6	306.4
Mean	3.81	38.3	-266.8	312.5
Stddev	0.16	1.7	2.5	10.4

Tropically (latitudes within 30° of the Equator) averaged quantities related to the global hydrological cycle. For the observations, the GSMaP (v7) retrieval is used for precipitation, P ; precipitable water, PW, is calculated only over the ocean for which observational estimates are taken from GMI. Top-of-atmosphere net solar, I_{solar} , and thermal infrared I_{thermal} irradiances are taken from the CERES SYN1deg daily Terra and Aqua product. For precipitation and precipitable water, ARPEGE-NH is excluded from the calculation of the multi-model mean

couples most directly to the circulation. The column water burden is only calculated over the ocean, to better enable comparisons with observations. Compared to the observations, the simulations appear somewhat less cloudy, as on average they are radiating thermal energy to space at a slightly greater rate than observed, but also absorbing a commensurately larger amount of solar energy. The net imbalance is quite close to observed, but differences among models can be large. NICAM-3.5 km simulates energy being absorbed at about twice the rate simulated by ICON (67.8 W m⁻² versus 31.1 W m⁻²). Such differences notwithstanding, given that this was the first time most of these models were ever run in such a configuration, and that no effort has been made to match the observations, we judge the degree of similitude with the observations as encouraging.

In analyzing the precipitation fields emerging from the DYAMOND simulations, a global 24-h cycle, whose peak-to-peak amplitude is 10 % of the mean, robustly emerged in the time series of each of the simulations. This is a feature of the climate system that we were not previously aware of. The day-to-day consistency of the feature was sufficiently robust to be identifiable in the composite 24-h cycle (in UTC time) of global precipitation (Fig. 6).

Globally, precipitation in the simulations peaks when the sun is in the western hemisphere, around 2000 UTC in most models, albeit somewhat earlier (nearer 1500 UTC) in SAM-4.3 km and NICAM-3.5 km. GSMaP (v7) precipitation retrievals are noisier, but are also indicative of a 24-h cycle peaking when the sun is in the western hemisphere. As far as the minimum in precipitation is concerned, which according to retrievals occurs between 0700 and 1000 UTC, all models tend to show a similar feature somewhat earlier. Locally, over land, it is well known that convective precipitation tends to peak in the late afternoon or early evening, while over ocean the peak is more in the morning hours. The simulated and observed 24-h cycle thus reflects the inhomogeneous distribution of precipitation zonally, where a peak near 2000 UTC would arise from the synchronization of precipitation maximizing over the warmer waters around the Maritime Continent (Warm Pool) with that over Africa. The slightly earlier peak in precipitation from NICAM-3.5 km and SAM-4.3 km may imply a greater contribution of precipitation from the monsoon regions of South Asia.

Predictability

Tropical cyclones

Given the very large data volumes involved, for the purposes of this study, we identified tropical cyclones with the help of an algorithm that searched for contiguous and non-stationary tracks defined by a minimum in the surface pressure, over the ocean, equatorward of 30°. Tracks lasting more than 1.5 days and with a minimum along track surface pressure less than 985 hPa were identified as tropical cyclones. The chosen threshold is slightly lower than that 994 hPa used to track cyclones in output from coarser resolution models (Roberts et al. 2015). For consistency across the models, the analysis was performed on each model's surface pressure fields after first being remapped to the standard 0.1° grid, masking land points using the CDO land-sea mask³, and with a 6-h time increment. To test this simple approach, it was compared to a more comprehensive algorithm (Kodama et al. 2015), based on the three-dimensional temperature and wind fields, applied to 30 years of data from a previous 14-km NICAM simulation. Application of the simple algorithm to the NICAM output resulted in an identification of nearly 90 % of the tropical cyclones identified by the more complex algorithm.

The algorithm was applied to the entire 40-day period for 8 simulations, resulting in the identification of 76 tropical cyclones, or just over 9 per simulation. The track of each tropical cyclone identified by the algorithm is shown in Fig. 7. The median number of identified tropical cyclones was 8.5. As compared to the other simulations, GEOS-3.3 km output is an outlier, in that it identified twenty tropical cyclones. In reality, between 1 August and 10 September 2016, 14 tropical cyclones with $P_{s,min} \leq 985$ hPa formed—8 in the western North Pacific (WNP) and 3 each in the eastern North Pacific (ENP) and Atlantic. One deep depression, but no cyclones, formed in the Northern Indian Ocean during this period. When limiting the classification to stronger tropical cyclones $P_{s,min} \leq 970$ hPa, the models identified 3 to 7 (mean of 4.9) tropical cyclones each⁴ (mean of 2.7 in WNP, 0.7 in Atlantic, 1.5 in ENP). In reality, six cyclones with $P_{s,min} \leq 970$ hPa formed during this period, three (Lionrock, Namtheun, Meranti) in the WNP, two in the ENP, and one (Gaston) in the Atlantic. Among the simulations, ARPEGE-2.5 km produces unrealistically strong cyclones; five tropical cyclones had $P_{s,min} \leq 900$ hPa, and the tropical cyclone it formed in the Gulf of Mexico saw its pressure drop to 845 hPa; a value 25 hPa lower than the lowest ever recorded in a tropical cyclone. To explore this issue, an extra simulation of a few days was performed with ARPEGE-2.5 km using the corrected setting for the evaporation coefficient. This simulation leads to substantially less deepening and explains most, if not all, of the difference as compared to the other models. Given the obvious question marks (tropical cyclone strength in ARPEGE-2.5 km and number in GEOS), and keeping in mind limitations in the present approach to tracking, the similitude between the observations and the simulations is surprisingly large and encouraging of further research.

Integrated water vapor

In the tropics, precipitation and circulation are very tightly coupled, and column water is a very good indicator of precipitation (Bretherton et al. 2004; Peters and Neelin 2006; Mapes et al. 2018). These qualities, combined with sharp spatial gradients in the vicinity of precipitation, identify column water vapor as an interesting quantity for prediction—something of a tropical analogue to the mid-troposphere geopotential field in the extra tropics. Using the DYAMOND models, we explore some aspects of the predictability of this (and other fields) for simulations in which the tropical dynamics are not distorted by the well-known deficiencies of parameterized convection. Similar questions have been explored before

³Some outliers associated with persistent features with anomalously low pressure (< 840 hPa) were additionally filtered (mostly in the FV3 output), as these were believed to arise from cyclones interacting with land which were not filtered by the CDO land mask.

⁴Excluding GEOS-3.3 km which identified 15 strong cyclones.

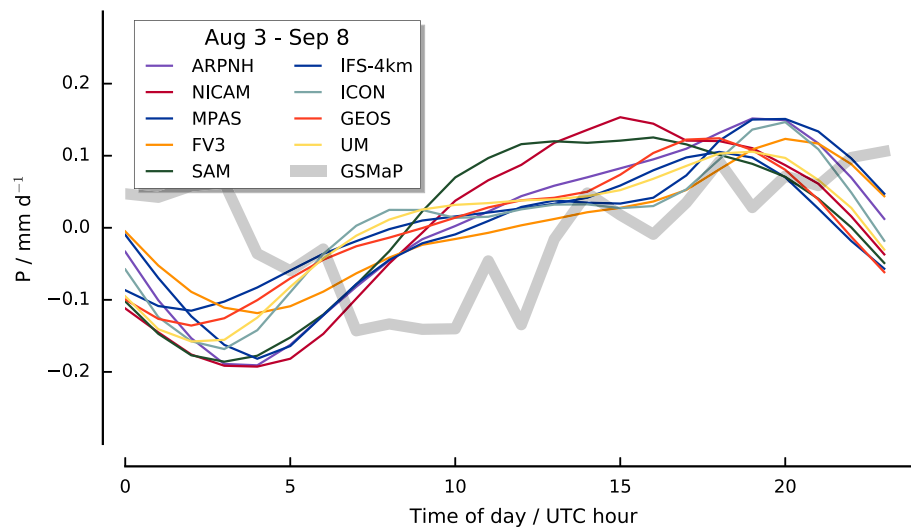


Fig. 6 Composite diurnal cycle of global precipitation as anomaly from mean

using a single model (e.g., Mapes et al. (2008), Bretherton and Khairoutdinov (2015), Judt (2018)), and this is the first time that they have been explored using a realistic surface orography and with an ensemble of different models.

Both Mapes et al. (2008) and Bretherton and Khairoutdinov (2015) measured error growth through the growth of (nearly) infinitesimal differences in precipitable water between pairs of otherwise identical runs. They showed that this measure of error growth saturates on small scales after about 2 to 4 days. At larger scales, and hence globally, it saturates after 14 to 30 days. On no scale could these studies discern a difference between the tropics and extra-tropics. Judt (2018) did not address the difference between tropical and extra-tropical error growth, but showed that—unlike for water vapor—the growth of perturbation energy increases relatively more rapidly at smaller scales, where the kinetic energy spectrum is relatively flatter ($k^{-5/3}$).

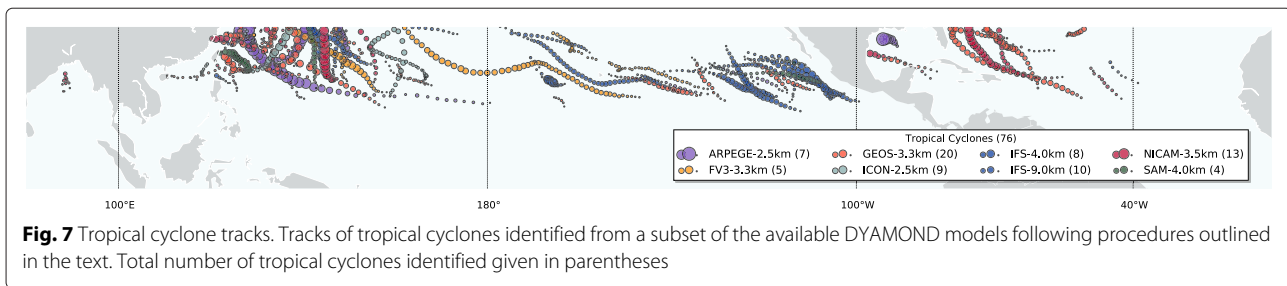
The DYAMOND simulations are consistent with the earlier analysis, though a hint of extended predictability in the tropics merits further analysis. This conclusion is drawn from Fig. 8 which presents the zonally averaged anomaly column water vapor covariance between a pair of models (ICON-2.5 km and FV3-3.3 km) as a function of latitude. The covariance (normalized at each latitude by the mean variance of ICON at that latitude) decays with time—as expected from the chaotic dynamics of the atmosphere. After about 14 days, the covariance has decayed to near zero suggesting that the ability of one model to predict the other's evolution has an envelope of about 2 weeks. This is indicative of somewhat less predictability

than found from the single model aqua-planet studies of previous investigators. The envelope of positive covariance (green colors) appears slightly more extended with time toward the Equator, suggesting that the chaotic dynamics may scramble signals in these regions somewhat less efficiently.

These questions are pursued more quantitatively by comparing the decay of the global mean covariance across pairs of models, and among perturbation experiments using slightly different configurations of a single model, in this case ICON-2.5 km and two simulations with ICON-5 km. The latter is more akin to experiments analyzed in the earlier literature and as discussed above. This analysis, Fig. 9, confirms the impression of a roughly 2-week envelope of coherence across the models. Simulations with slight perturbations in the configuration of ICON, however, show longer coherence, suggesting an intrinsic predictability limit approaching 3 weeks—more consistent with earlier studies. The slight pick up of covariability after about 5 weeks may be due to the seasonal cycle or a signature of intraseasonal variability. The additional data from the accidental ensemble offers additional opportunities to explore these issues. Looking across the simulations to identify if particular features (like envelopes of tropical cyclone genesis, or breaks in the monsoon) are predictable with longer lead times might help to identify additional sources of predictability, as discussed by Fudeyasu et al. (2008) among others.

Summary and outlook

Before the start of the DYAMOND project, the feasibility of performing global storm-resolving models



had been well demonstrated (e.g., Tomita et al. (2005), Satoh et al. (2008)). The simulations described here, performed by nine different groups from six national entities across three continents, demonstrate that such simulations have now gone from being feasible to practical.

With the increasing practicality of such simulations, it becomes possible to begin answering some basic questions. For instance, how sensitive are the simulations to a particular implementation? Before DYAMOND, most of the global storm-resolving models used here had never been run in this configuration, and no two models had ever before attempted to perform the same simulations. Based on our preliminary analysis, we find that basic aspects of the general circulation are well captured by the storm-resolving models. The outgoing long-wave radiation is well simulated, as is the global precipitation and distribution of precipitable water. Agreement among the models is such that it is difficult to establish if differences with observations—for instance, more precipitation in the poleward flank of the storm tracks and in the equatorial region just south of the Equator—represent deficiencies in the models or in the retrievals of these quantities. The visual representation of clouds is, from a geostationary field of view, practically indistinguishable from observations. Insofar as it can be determined given the brevity of the simulations and the basic storm-tracking algorithm, the tropical genesis and intensification statistics of tropical cyclones are well captured. About the right number of tropical cyclones form in about the right place and intensify in about the right proportion. Despite its very different dynamics, the simulations suggest that predictability time scales in the tropics are similar, or perhaps even slightly longer, than in the mid-latitudes. Finally, we identify a diurnal cycle in global precipitation that is consistent across all simulations and similarly evident in the observations. Considering that the models were not specifically tuned for this case and that minor implementation errors are to be expected given the early stage of the development, this agreement is remarkable.

The simulations are not without their deficiencies. Even the present, relatively superficial, analysis makes

clear that to reap the rewards of being able to simulate the general circulation of Earth's global atmosphere at storm-resolving scales, some unconstrained degrees of freedom remain to be tamed. Our preliminary analysis identifies challenges in linking energy and water budgets, as evidenced by differences in shortwave (solar) irradiances at top-of-atmosphere, a quantity that is likely to be influenced by the representation of (often shallow) clouds, turbulence, and cloud microphysical processes. However, by virtue of the ability of GSRMs to directly link these processes to the circulation on the one hand, and observations at similar scales on the other, we are optimistic that research targeted at addressing these challenges will bear fruit. If so, GSRMs will provide an improved physical foundation for model-based investigations of Earth's climate and climate change and usher in a new generation of climate models. With their ability to explicitly resolve convective storms, GSRMs may also transform the weather prediction enterprise and lead to improved forecasts of severe weather from local to global scales.

Another important motivation for the DYAMOND project was to address performance and analysis bottlenecks associated with global storm-resolving models. Our experiences across a variety of architectures with a variety of models suggest that a throughput of 6 to 10 days per day is feasible on a small 10 to 20 % of present day (tier 1) machines. GSRMs with O (3 km) global grids can be expected to reach a throughput of 100 simulated days per day in the coming few years—even without disruptive changes to programming paradigms (cf Neumann et al. (2019)). This rate of throughput makes such models applicable to a wider range of climate questions. Post-processing of the massive amounts of output from such models is challenging, both by virtue of its sheer volume and because of the more complex grid structures used by many models. In dealing with this output, domain-specific analysis tools, like the CDOs, proved to be invaluable. Our experience was, in contrast to what is commonly believed, that different output strategies, file names, variable names, units, etc. were not a great impediment to analysis, but that having standard conforming data *dimensions* is essential for reaping the benefits of

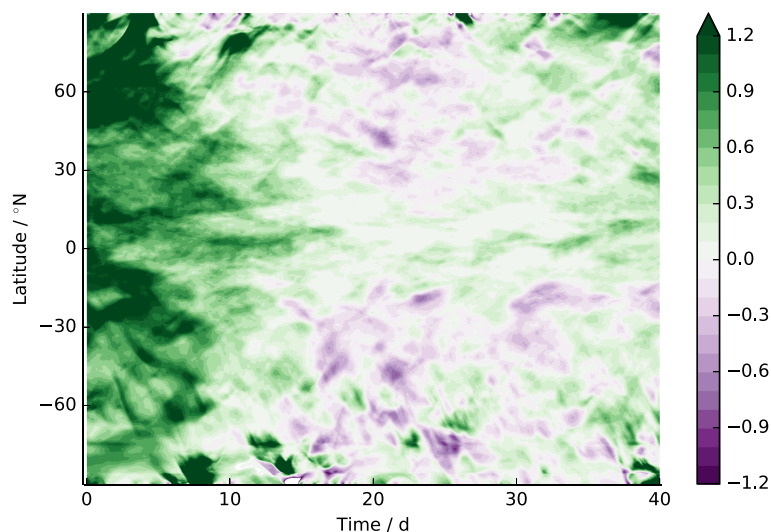


Fig. 8 Water vapor anomaly correlation. Zonally averaged anomaly correlation of hourly (0.1 degree) precipitable water between ICON-2.5 km and GEOS-3.3 km normalized by zonally and temporally averaged water vapor variance from ICON-2.5 km plotted as a function of time and latitude

domain-specific analysis tools. Use of compressed data formats greatly reduced the data volumes, but was subject to the dynamic range of the data, which in some cases was artificially inflated by inadequate filtering of insignificant values.

Any attempt to give a comprehensive overview of models that contain such a fantastic range of scales for a fluid whose dynamics are as diverse and heterogeneous as Earth's atmosphere will be necessarily superficial. Our hope is that by documenting the DYAMOND simulations,

curating subsets of their output, and by making this, as well as their full output, available for analysis by the broader research community, a more specific, and thereby in-depth, analysis will follow. Toward this end, we have also used this manuscript to highlight differences in model formulation which makes their comparison interesting, as well as features of the simulations that we noticed and believe merit further study. To organize the dissemination of findings from studies of these and related questions, a subset of the present authors have also organized a

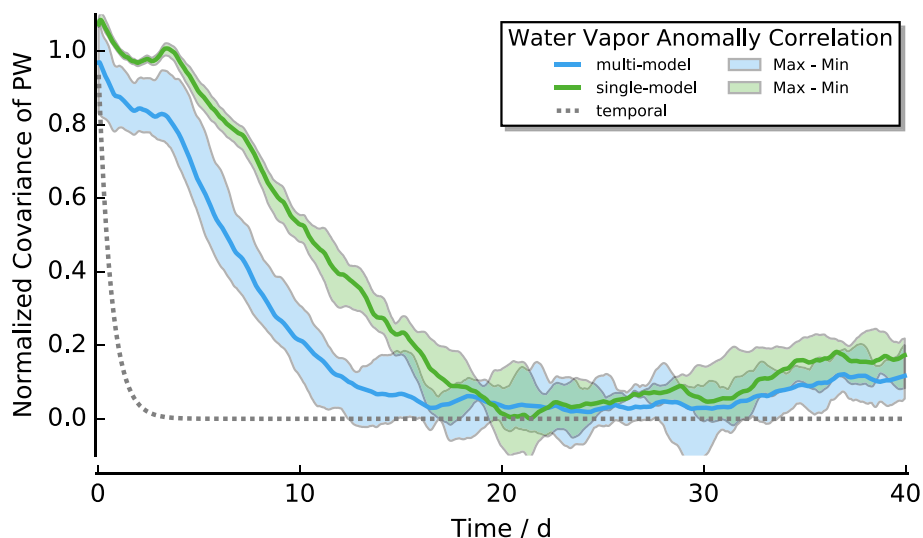


Fig. 9 Temporal decrease of globally averaged water vapor anomaly correlation. The intermodel decay is for the 3 ICON-2.5 km and 2 versions of the ICON-5.0 km model, and intramodel decay is from 11 pairs of models

special issue of the *Journal of the Meteorological Society of Japan*⁵. We hope that it will also help nucleate interest into a new generation of models that many of us believe offers the best, and perhaps only, chance to resolve long-standing biases in conventional representations of the climate system.

Abbreviations

DKRZ: German Climate Computing Center; ECMWF: European Centre for Medium-range Weather Forecasts; GEOS: Goddard Earth Observing System; GSRM: Global storm-resolving Model; ICON: Icosahedral non-hydrostatic model; IFS: Integrated Forecast System of the ECMWF; MPAS: Model for Predicting Across Scales; NICAM: Non-hydrostatic Icosahedral Atmospheric Model; SAM: Global System for Atmospheric Modeling; UM: Unified model of the United Kingdom's Meteorological Service

Acknowledgements

BS thanks the AORI at the University of Tokyo who supported an extended visit to the University of Tokyo which facilitated the writing of this manuscript. Prof. Yukari Takayabu is thanked for her input on and provision of the GSMaPv6 precipitation retrievals. The NICAM simulations were performed on the Earth Simulator at the Japan Agency for Marine-Earth Science and Technology (JAMSTEC). Peter Caldwell is thanked for constructive comments on an earlier draft.

Authors' contributions

MS and BS conceived of the project, and together with JB and CSB designed the study. LA, XC, PD, FJ, DK, LK, MK, WP, JLS, RS, BV, PLV, NW, and LZ performed or contributed to the simulations described in the manuscript. NR provided the scientific visualization and drafted Figs. 1–4. PN developed and lead the data infrastructure and performance review of the models. DK, BS, and CK performed the analysis. BS wrote the manuscript incorporating input from all authors. All authors read and approved the final manuscript.

Funding

This work was supported by the Max Planck Society, the European Union's Horizon 2020 research and innovation program under grant agreement ESIWACE No 675191, and the High-Definition Clouds and Precipitation for Climate Prediction (HD(CP)²) project of the German Ministry for Education and Research (BMBF) within the framework program "Research for Sustainable Development (FONA)", www.fona.de, under the number FKZ: 01LK1211A/C. MS, CK, and RS are supported by the FLAGSHIP2020 within the priority study4 (Advancement of meteorological and global environmental predictions utilizing observational "Big Data") and the "Integrated Research Program for Advancing Climate Models (TOUGOU program)" from the Ministry of Education, Culture, Sports, Science and Technology (MEXT), Japan. Marat Khairoutdinov was supported by the NSF Grant AGS1418309 to Stony Brook University, and also by the NCAR-Wyoming Supercomputing Center, where SAM simulation was performed.

Availability of data and materials

Model output supporting the conclusions of this article are archived by the German Climate Computing Centre (DKRZ) and made available through the ESIWACE project (<https://www.esiwace.eu/services/diamond>).

Competing interests

The authors declare that they have no competing interest.

Author details

¹Max Planck Institute for Meteorology, Bundesstraße 53, 20146, Hamburg, Germany. ²Atmosphere and Ocean Research Institute, The University of Tokyo, 5-1-5 Kashiwanoha, Kashiwa, Chiba, 277-8564, Japan. ³CNRM Météo-France, 42 av. G. Coriolis, 31057 Toulouse Cedex 1, France. ⁴German Climate Computing Center, DKRZ, Bundesstrasse 45a, 20146, Hamburg, Germany. ⁵Department of Atmospheric Sciences, University of Washington, Box 351640, Seattle, WA, 98195-1640, USA. ⁶Geophysical Fluid Dynamics Laboratory, Princeton University, Forrestal Campus/U.S. Route 1, P.O. Box 308, Princeton, NJ, 08542, USA. ⁷ECMWF, Shinfield Road, Reading, RG2 9AX, UK. ⁸National Center for

Atmospheric Research, PO Box 3000, Boulder, CO, 80303-3000, USA. ⁹School of Marine and Atmospheric Sciences, Stony Brook University, Stony Brook, NY, 11794-5000, USA. ¹⁰Hans-Ertel-Zentrum für Wetterforschung, Deutscher Wetterdienst, Frankfurterstrasse 135, Offenbach, Germany. ¹¹Japan Agency for Marine-Earth Science and Technology, 3173-15, Showa-machi, Kanazawa-ku, Yokohama, Kanagawa, 236-0001, Japan. ¹²NASA Global Modeling and Assimilation Office, Goddard Space Flight Center, Greenbelt, Maryland, USA. ¹³National Centre for Atmospheric Science, University of Reading, Reading, UK.

Received: 2 March 2019 Accepted: 28 July 2019

Published online: 30 September 2019

References

- Bessho K, Date K, Hayashi M, Ikeda A, Imai T, Inoue H, Kumagai Y, Miyakawa T, Murata H, Ohno T, Okuyama A, Oyama R, Sasaki Y, Shimazu Y, Shimoji K, Sumida Y, Suzuki M, Taniguchi H, Tsuchiyama H, Uesawa D, Yokota H, Yoshida R (2016) An introduction to Himawari-8/9 –Japan's new-generation geostationary meteorological satellites. *J Meteorol Soc Jpn* 94(2):151–183. <https://doi.org/10.2151/jmsj.2016-009>
- Bethel EW, Childs H, Hansen C (2012) High performance visualization: enabling extreme-scale scientific insight. Chapman & Hall/CRC, New York. <https://doi.org/10.1201/b12985>
- Bony S, Stevens B, Frierson DMW, Jakob C, Kageyama M, Pincus R, Shepherd TG, Sherwood SC, Siebesma AP, Sobel AH, Watanabe M, Webb MJ (2015) Clouds, circulation and climate sensitivity. *Nat Geosci* 8(4):261–268
- Bretherton CS, Peters ME, Back LE (2004) Relationships between water vapor path and precipitation over the tropical oceans. *J Clim* 17(7):1517–1528
- Bretherton CS, Khairoutdinov MF (2015) Convective self-aggregation feedbacks in near-global cloud-resolving simulations of an aquaplanet. *J Adv Model Earth Syst* 7(4):1765–1787
- Bubnová R, Hello G, Bénard P, Geleyn J-F (1995) Integration of the fully elastic equations cast in the hydrostatic pressure terrain-following coordinate in the framework of the arpege/aladin nwp system. *Mon Weather Rev* 123(2):515–535
- Clyne J, Mininni P, Norton A, Rast M (2007) Interactive desktop analysis of high resolution simulations: application to turbulent plume dynamics and current sheet formation. *New J Phys* 9(8):301
- Cotton WR, Tripoli GJ (1978) Cumulus convection in shear flow—three-dimensional numerical experiments. *J Atmos Sci* 35(8):1503–1521
- Fudeyasu H, Wang Y, Satoh M, Nasuno T, Miura H, Yanase W (2008) Global cloud-system-resolving model NICAM successfully simulated the lifecycles of two real tropical cyclones. *Geophys Res Lett* 35(22):2397–6
- Hohenegger C, Kornbluh L, Becker T, Cioni G, Engels JF, Klocke D, Schulzweida U, Stevens B (2019) Convergence of zero order climate statistics in global simulations using explicit convection. *J Meteorol Soc Jpn*
- Ito J, Hayashi S, Hashimoto A, Ohtake H, Uno F, Yoshimura H, Kato T, Yamada Y (2017) Stalled improvement in a numerical weather prediction model as horizontal resolution increases to the sub-kilometer scale. *SOLA* 13(0):151–156
- Jubair MI, Alim U, Röber N, Clyne J, Mahdavi-Amiri A (2016) Icosahedral maps for a multiresolution representation of earth data. In: VMV '16 Proceedings of the Conference on Vision, Modeling and Visualization, Bayreuth. pp 161–168
- Judt F (2018) Insights into atmospheric predictability through global convection-permitting model simulations. *J Atmos Sci* 75(5):1477–1497
- Khairoutdinov MF, Randall DA (2003) Cloud resolving modeling of the ARM summer 1997 IOP: model formulation, results, uncertainties, and sensitivities. *J Atmos Sci* 60(4):607–625
- Klemp JB, Wilhelmson RB (1978) The simulation of three-dimensional convective storm dynamics. *J Atmos Sci* 35(6):1070–1096
- Klocke D, Brueck M, Hohenegger C, Stevens B (2017) Rediscovery of the doldrums in storm-resolving simulations over the tropical Atlantic. *Nat Geosci* 10(1):153–7
- Kodama C, Noda AT, Satoh M (2012) An assessment of the cloud signals simulated by NICAM using ISCCP, CALIPSO, and CloudSat satellite simulators. *J Geophys Res-Atmos* 117(D12):1–17
- Kodama C, Yamada Y, Noda AT, Kikuchi K, Kajikawa Y, Nasuno T, Tomita T, Yamaura T, Takahashi HG, Hara M, Kawatani Y, Satoh M, Sugi M (2015) A 20-year climatology of a nicam amip-type simulation. *J Meteorol Soc Japan* 93(4):393–424. <https://doi.org/10.2151/jmsj.2015-024>

⁵https://jmsj.metsoc.jp/CallForPaper_2019JMSJ_DYAMOND.pdf

- Kubota T, Shige S, Hashizume H, Aonashi K, Takahashi N, Seto S, Hirose M, Takayabu YN, Ushio T, Nakagawa K, Iwanami K, Kachi M, Okamoto K (2007) Global precipitation map using satellite-borne microwave radiometers by the gsmmap project: production and validation. *IEEE Trans Geosci Remote Sens* 45(7):2259–2275. <https://doi.org/10.1109/TGRS.2007.895337>
- Langhans W, Schmidli J, Schär C (2012) Bulk convergence of cloud-resolving simulations of moist convection over complex terrain. *J Atmos Sci* 69(7):2207–2228
- Lin S-J, Rood RB (2004) A “vertically Lagrangian” finite-volume dynamical core for global models. *Mon Weather Rev* 132(544):2293–307
- Malardel S, Wedi N, Deconinck W, Diamantakis M, Kuehnlein C, Mozdzyński G, Hamrud M, Smolarkiewicz P (2016) A new grid for the IFS. *ECMWF Newsl* 146:23–28. <https://doi.org/doi:10.21957/zwdu9u5i>
- Mapes B, Tulich S, Nasuno T, Satoh M (2008) Predictability aspects of global aqua-planet simulations with explicit convection. *J Meteorol Soc Jpn Ser II* 86A:175–185
- Mapes BE, Chung ES, Hannah WM, Masunaga H, Wimmers AJ, Velden CS (2018) The meandering margin of the meteorological moist tropics. *Geophys Res Lett* 45(2):1177–1184
- Marotzke J, Jakob C, Bony S, Dirmeyer PA, O’Gorman PA, Hawkins E, Perkins-Kirkpatrick S, Le Quere C, Nowicki S, Paulavets K, Seneviratne SI, Stevens B, Tuma M (2017) Climate research must sharpen its view. *Nat Clim Chang* 7(2):89–91
- Matsuno T (2016) Prologue: tropical meteorology 1960–2010—personal recollections. *Meteorol Monogr* 56. <https://journals.ametsoc.org/doi/pdf/10.1175/AMSMONOGRAPH5-D-15-0012.1> <https://doi.org/10.1175/AMSMONOGRAPH5-D-15-0012.1>
- Mengaldo G, Wyszogrodzki A, Diamantakis M, Lock S-J, Giraldo FX, Wedi NP (2018) Current and emerging time-integration strategies in global numerical weather and climate prediction. *Arch Comput Methods Eng* 1–22. <https://doi.org/10.1007/s11831-018-9261-8>
- Neumann P, Dueben P, Adamidis P, Bauer P, Brueck M, Kornbluh L, Klocke D, Stevens B, Wedi N, Biercamp J (2019) Assessing the scales in numerical weather and climate predictions: will exascale be the rescue? *Phil Trans R Soc* 377:20180148. <https://doi.org/10.1098/rsta.2018.0148>
- Palmer TN (2016) A personal perspective on modelling the climate system. *Proc R Soc A* 472(2188):20150772–14
- Peters O, Neelin JD (2006) Critical phenomena in atmospheric precipitation. *Nat Phys* 2(6):393–396
- Phillips NA (1956) The general circulation of the atmosphere: a numerical experiment. *QJR Meteorol Soc* 82(352):123–164
- Putman WM, Lin S-J (2007) Finite-volume transport on various cubed-sphere grids. *J Comput Phys* 227(1):55–78
- Putman WM, Suarez M (2011) Cloud-system resolving simulations with the NASA Goddard Earth Observing System global atmospheric model (GEOS-5). *Geophys Res Lett* 38(16)
- Randall D, Khairoutdinov M, Arakawa A, Grabowski W (2003) Breaking the cloud parameterization deadlock. *Bull Am Meteorol Soc* 84(11):1547–1564
- Roberts MJ, Vidale PL, Mizielinski MS, Demory M-E, Schiemann R, Strachan J, Hodges K, Bell R, Camp J (2015) Tropical cyclones in the UPSCALE ensemble of high-resolution global climate models*. *J Clim* 28(2):574–596
- Rodwell MJ, Palmer TN (2007) Using numerical weather prediction to assess climate models 133(622):129–146
- Saito K, Ishida J-I, Aranami K, Hara T, Segawa T, Narita M, Honda Y (2007) Nonhydrostatic Atmospheric Models and Operational Development at JMA. *J Meteorol Soc Jpn Ser II* 85B:271–304
- Satoh M, Tomita H, Miura H, Iga S, Nasuno T (2005) Development of a global cloud resolving model - a multi-scale structure of tropical convections -. *J Earth Simul* 3:11–19
- Satoh M, Matsuno T, Tomita H, Miura H, Nasuno T, Iga S (2008) Nonhydrostatic icosahedral atmospheric model (NICAM) for global cloud resolving simulations. *J Comput Phys* 227(7):3486–3514
- Satoh M, Tomita H, Yashiro H, Miura H, Kodama C, Seiki T, Noda AT, Yamada Y, Goto D, Sawada M, Miyoshi T, Niwa Y, Hara M, Ohno T, Iga S-i, Arakawa T, Inoue T, Kubokawa H (2014) The Non-hydrostatic Icosahedral Atmospheric Model: description and development. *Prog Earth Planet Sci* 1:18. <https://doi.org/10.1186/s40645-014-0018-1>
- Satoh M, Tomita H, Yashiro H, Kajikawa Y, Miyamoto Y, Yamaura T, Miyakawa T, Nakano M, Kodama C, Noda AT, Nasuno T, Yamada Y, Fukutomi Y (2017) Outcomes and challenges of global high-resolution non-hydrostatic atmospheric simulations using the K computer. *Prog Earth Planet Sci* 4:13. <https://doi.org/10.1186/s40645-017-0127-8>
- Satoh M, Noda AT, Seiki T, Chen Y-W, Kodama C, Yamada Y, Kuba N, Sato Y (2018) Toward reduction of the uncertainties in climate sensitivity due to cloud processes using a global non-hydrostatic atmospheric model. *Prog Earth Planet Sci* 5:67. <https://doi.org/10.1186/s40645-018-0226-1>
- Satoh M, Stevens B, Jüdt F, Khairoutdinov M, Lin S-J, Putman WM, Düben P (2019) Global cloud resolving models. *Curr Clim Change Rep*. <https://doi.org/10.1007/s40641-019-00131-0>
- Skamarock WC, Klemp JB, Duda MG, Fowler LD, Park S-H, Ringler TD (2012) A Multiscale Nonhydrostatic Atmospheric Model Using Centroidal Voronoi Tessellations and C-Grid Staggering. *Mon Weather Rev* 140(9):3090–3105
- Skamarock WC, Park S-H, Klemp JB, Snyder C (2014) Atmospheric Kinetic Energy Spectra from Global High-Resolution Nonhydrostatic Simulations. *J Atmos Sci* 71(11):4369–4381
- Smagorinsky J (1963) General circulation experiments with the primitive equations. *Mon Weather Rev* 91(3):99–164
- Stevens B, Bony S (2013) What Are Climate Models Missing? *Science* 340(6136):1053–1054
- Stevens B, Ament F, Bony S, Crewell S, Ewald F, Gross S, Hansen A, Hirsch L, Jacob M, Kölling T, Zinner T, Mayer B, Wendisch M, Wolf K, Ehrlich A, Farrell D, Forde M, Jansen F, Konow H, Wing AA, Klingebiel M, Wirth M, Brueck HM, Bauer-Pfundstein M, Delanoë J, Rapp M, Rapp AD, Hagen M, Peters G, Bakan S, Klepp C (2019) A high-altitude long-range aircraft configured as a cloud observatory— the NARVAL expeditions. *Bull Amer Meteorol Soc*
- Tomita H, Tsugawa M, Satoh M, Goto K (2001) Shallow Water Model on a Modified Icosahedral Geodesic Grid by Using Spring Dynamics. *J Comput Phys* 174(2):579–613
- Tomita H, Satoh M (2004) A new dynamical framework of nonhydrostatic global model using the icosahedral grid. *Fluid Dyn Res* 34(6):357–400. <https://doi.org/10.1016/j.fluidyn.2004.03.003>
- Tomita H, Miura H, Iga S, Nasuno T, Satoh M (2005) A global cloud-resolving simulation: Preliminary results from an aqua planet experiment. *Geophys Res Lett* 32(8):3283
- Voldoire A, Decharme B, Pianezze J, Lebeaupin Brossier C, Sevault F, Seyfried L, Garnier V, Bielli S, Valcke S, Alias A, et al. (2017) Surfer v8.0 interface with oasis3-mct to couple atmosphere with hydrology, ocean, waves and sea-ice models, from coastal to global scales. *Geosci Model Dev* 10(11):4207–4227
- Walters D, Baran A, Boutle I, Brooks M, Earnshaw P, Edwards J, Furtado K, Hill P, Lock A, Manners J, Morcrette C, Mulcahy J, Sanchez C, Smith C, Stratton R, Tennant W, Tomassini L, Van Weverberg K, Vosper S, Willett M, Browse J, Bushell A, Dalvi M, Essery R, Gedney N, Hardiman S, Johnson B, Johnson C, Jones A, Mann G, Milton S, Rumbold H, Sellar A, Ujiie M, Whittall M, Williams K, Zerroukat M (2017) The Met Office Unified Model Global Atmosphere 7.0/7.1 and JULES Global Land 7.0 configurations. *Geosci Model Dev Discuss* 2017:1–78
- Wedi NP (2014) Increasing horizontal resolution in numerical weather prediction and climate simulations: illusion or panacea? *Philos Trans R Soc A Math Phys Eng Sci* 372(2018):20130289–20130289
- Weisman ML, Skamarock WC, Klemp JB (1997) The Resolution Dependence of Explicitly Modeled Convective Systems. *Mon Weather Rev* 125(4):527–548
- Williamson DL (2005) Moisture and temperature balances at the Atmospheric Radiation Measurement Southern Great Plains Site in forecasts with the Community Atmosphere Model (CAM2). *J Geophys Res-Atmos* 110(D15):3123–17
- Williamson DL (2007) The Evolution of Dynamical Cores for Global Atmospheric Models. *J Meteorol Soc Jpn Ser II* 85B:241–269
- Williams KD, Bodas-Salcedo A, Déqué M, Fermepin S, Medeiros B, Watanabe M, Jakob C, Klein SA, Senior CA, Williamson DL (2013) The Transpose-AMIP II Experiment and Its Application to the Understanding of Southern Ocean Cloud Biases in Climate Models. *J Clim* 26(10):3258–3274
- Wood N, Staniforth A, White A, Allen T, Diamantakis M, Gross M, Melvin T, Smith C, Vosper S, Zerroukat M, Thuburn J (2013) An inherently mass-conserving semi-implicit semi-Lagrangian discretization of the deep-atmosphere global non-hydrostatic equations. *QJR Meteorol Soc* 140(682):1505–1520
- Zängl G, Reinert D, Rípodas P, Baldauf M (2014) The ICON (ICOahedral Non-hydrostatic) modelling framework of DWD and MPI-M: Description of the non-hydrostatic dynamical core. *QJR Meteorol Soc* 141(687):563–579

Publisher's Note

Springer Nature remains neutral with regard to jurisdictional claims in published maps and institutional affiliations.